

The non-homogeneous flow of a thixotropic fluid around a sphere

Jaekwang Kim¹, and Jun Dong Park^{2,*}

¹Department of Mechanical Science & Engineering,
University of Illinois at Urbana–Champaign, Urbana, Illinois, 61801

²Department of Chemical Engineering,
Kumoh National Institute of Technology, Gumi, Gyeongbuk, 39177
jk12@illinois.edu, jdp@kumoh.ac.kr

*corresponding author

Abstract

The non-homogeneous flow of a thixotropic fluid around a settling sphere is simulated. A four-parameter Moore model is used for a generic thixotropic fluid and discontinuous Galerkin method is employed to solve the structure-kinetics equation coupled with the conservation equations of mass and momentum. Depending on the normalized falling velocity U^* , which compares the time scale of structure formation and destruction, flow solutions are divided into three different regimes, which are attributed to an interplay of three competing factors: Brownian structure recovery, shear-induced structure breakdown, and the convection of microstructures. At small U^* ($\ll 1$), where the Brownian structure recovery is predominant, the thixotropic effect is negligible and flow solutions are not too dissimilar to that of a Newtonian fluid. As U^* increases, a remarkable structural gradient is observed and the structure profile around the settling sphere is determined by the balance of all three competing factors. For large enough U^* ($\gg 1$), where the Brownian structure recovery becomes negligible, the balance between shear-induced structure breakdown and the convection plays a decisive role in determining flow profile. To quantify the interplay of three factors, the drag coefficient C_s of the sphere is investigated for ranges of U^* . With this framework, the effect of the destruction parameter, the confinement ratio, and a possible nonlinearity in the model-form on the non-homogeneous flow of a thixotropy fluid have been addressed.

1 Introduction

Thixotropy is a distinct rheological phenomenon that formally signifies “the continuous decrease of viscosity with time when flow is applied to a material that has been previously at quiescent state, and the subsequent recovery of viscosity when flow ceases” [1]. Such time-history effect is to be differentiated from viscoelasticity in that the thixotropic material naturally recovers initial viscosity after cessation of flow [2]. The origin of thixotropy is associated with the gradual breakdown and building up of the microstructure [3].

Thixotropic materials are often encountered in industrial processes including mining, wastewater treatment, printing inks, oil pipeline-transport, consumer applications (e.g cosmetics and food) as well as biological fluids such as blood [4, 5, 6, 7, 8]. Occasionally, thixotropy has been intentionally built into commercial products for the convenience of their uses. For example, thixotropic behavior of printing and coating materials greatly facilitates whole processes from storage to application and drying. In the storage process, highly stable materials with large viscosity are required to prevent

sedimentation problem. By contrast, the application process requires flowable materials with low viscosity at high shear rates. In the following drying process, rapid recovery of the viscosity is needed, which plays a crucial role in the control of leveling and sagging problems [9]. Introducing thixotropy to such products makes it possible to satisfy these required conditions at each stage.

The ubiquity and growing importance of thixotropy leads to considerable effort to understand thixotropy of materials. Numerous studies have dealt with thixotropy with a variety of approaches. For instance, step experiments, hysteresis loops, and shear startup experiments have been typically employed in experimental approaches to characterize thixotropic fluids [10]. What lies at the heart of these studies is the understanding of the relationship between their rheology and microstructural change (e.g., size of the floc, alignment of fibers, spatial distribution, and entanglement density). Theoretical studies of thixotropy aim to interpret and predict the thixotropic behaviors of material. In this regard, numerous models have been proposed for thixotropy in literatures. Excellent reviews are available at other sources [10, 11], but in general, the existing thixotropy models are categorized into 3 groups; structural kinetics models [12, 13], continuum mechanical models [14, 15] and micro-mechanical models [16, 17].

Though previous studies have established well-grounded knowledge on thixotropy, practical application is often limited. Most experimental approaches on thixotropy mainly analyze material behavior at a homogeneous flow field (e.g. one-dimensional shear), which is induced from a few of commercialized flow geometries at rheometers. Likewise, many of the theoretical modeling works have been formulated under the assumption of homogeneous flow field as well. However, actual applications of thixotropic materials often include non-homogeneous flow fields. For example, mixing of thixotropic fluid is performed in various batches with complicated geometries that are designed for performance improvement. In the batches, a heterogeneous shear field develops at different positions due to geometrical hindrance [18, 19].

In the presence of such non-trivial geometrical factors, the material thixotropy shows not only time dependent but also spatial dependent behavior, because fluid elements accumulate different shear history according to different pathlines. Thus, previous studies can provide an insight solely on intrinsic thixotropy with some limitation on the knowledge on rheology in real flow scenarios. Consequently, the lack of understanding on non-homogeneous thixotropic fluid flows causes hardship for design and control of material process with thixotropy.

The specific aim of the present work is to obtain a basic idea for interpreting a non-homogeneous flow of thixotropic fluid. In a strict sense, many of materials of interest, such as bloods and drilling fluids, display behavior that is a combination of thixotropic, elastic and viscous properties. Therefore, it is more reasonable and realistic to adopt a sophisticated rheological model with viscoelasticity and time dependency. Such rheological behaviors may or may not be observed, depending on the magnitude of stress and the timescales of each properties compared to an observation timescale. In an effort to address this issue, a few studies have been conducted. These studies include modeling of thixo-elasto-visco-plastic (TEVP) fluid in circular contraction-expansion asymmetric pipe [20, 21, 22, 23]. It is novel and meaningful that these studies have provided quantitative solution for non-homogenous flow of TEVP fluid in a non-trivial flow geometry, which is challenging in terms of both rheology and numerical analysis. Meanwhile, the use of the sophisticated model makes it hard to separate thixotropic effect and viscoelastic effect, which prevents intuitive understanding on the role of each property. By narrowing our attention to purely-viscous thixotropic fluids, we seek to understand the interplay between thixotropy and fluid geometry. Such insight will be useful not only for understanding of more elaborated rheological behavior such as in TEVP fluid, but be readily extended to much more complicated flow scenarios in industrial material process. This specific goal makes current study distinct from other studies.

We consider a specific model problem, which is a steady thixotropic flow around a sedimenting

sphere in a cylindrical tube. This model problem has been considered as a canonical flow in computational rheology. For example, a wide range of works from the Non-Newtonian fluid mechanics community have investigated this flow scenario in the presence of shear-thinning and yield-stress [24, 25, 26], shear-thickening [27, 28], and viscoelasticity [29, 30]. When it comes to thixotropic fluids, both previous experimental [31, 32] and numerical [33] studies have mainly focused on the effect of material aging time on terminal velocity (or resistance) of a spherical particle. However, their analysis did not extend to illustrating how fluid dynamics of a material will interplay with other factors of thixotropy, such as non-homogenous shear-breakdown and the convection of microstructures. Aside from theoretical interest, the thixotropic flow around a sphere is also closely linked with various industrial and medical applications as well. Flow assurance and drilling of oil & gas wells are prime examples in industry [34], and blood clotting disorder [35] and dysphagia (difficulty in swallowing) [4] are highlighted topics in medical applications. We believe that the current work will provide a useful insight for analyzing relevant flow scenarios of ultimate interest.

The following Section 2 formulates a model problem and introduces characterizing dimensionless numbers. A brief description on an employed numerical method is also provided. In Section 3, simulation results are analyzed with relevant dimensionless numbers and a general framework for interpreting non-homogenous thixotropic flow is suggested. With this, we investigate the effect of destruction factor, the viscosity ratio of full-structured state to broken state, and confinement to a non-homogenous thixotropic flow in Section 4. Cases of nonlinear thixotropic models are presented in Section 5. Lastly, Section 6 summarizes the overall result and discuss future research direction for non-homogenous thixotropic flow.

2 Formulation

2.1 Structure-kinetics model

To model a generic thixotropic fluid, we employ the structure kinetics approach to thixotropy. In this approach, the instantaneous material structure is represented by means of a dimensionless scalar parameter λ , which determines the rheological properties of a material. Then, a structural evolution is introduced to delineate the rate of change in λ as a function of flow condition and current status of microstructure. Although the structure kinetics approach has some difficulty in clearly correlating the structure parameter λ to experimental measurements of the microstructure, it is favored for a generic thixotropy model because of the wide range and the complex nature of microstructures that can possibly be encountered in different types of thixotropic materials [3]. Indeed, it has been applied to a wide range of materials and provided effective interpretation and prediction of thixotropy.

In general, structure-kinetics models can be classified according to (a) the kinetic evolution equation for λ , (b) the basic constitutive equation, and (c) the manner in which the rheological parameters have been linked to the structural parameter [1]. In this work, we take a simple model-form that describes the basic thixotropic features. To begin with, we consider the linear structure-kinetics model [13] in a flow of velocity \mathbf{u} ,

$$\frac{d\lambda}{dt} = \frac{\partial\lambda}{\partial t} + (\mathbf{u} \cdot \nabla\lambda) = -k_d\dot{\gamma}_s\lambda + k_a(1 - \lambda), \quad (1)$$

where $\dot{\gamma}_s$ is the second-invariant of strain-rate tensor ($\dot{\boldsymbol{\gamma}} = \nabla\mathbf{u} + (\nabla\mathbf{u})^T$),

$$\dot{\gamma}_s = \sqrt{\frac{\dot{\boldsymbol{\gamma}} : \dot{\boldsymbol{\gamma}}}{2}}. \quad (2)$$

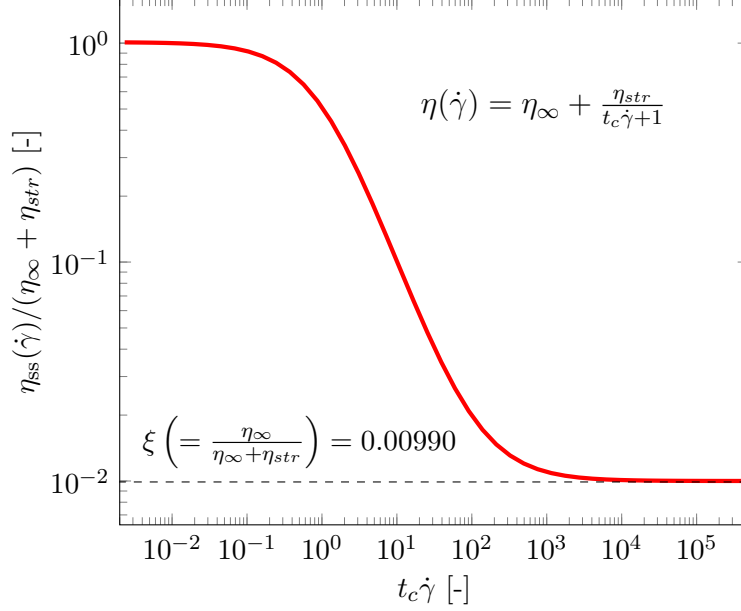


Figure 1: The steady state viscosity η_{ss} (4) of Moore thixotropy fluids in simple shear with the model parameters $\{\eta_\infty, \eta_{str}, k_a, k_d\}$ summarized in Table 1. The vertical line is normalized by $\eta_\infty + \eta_{str}$ and horizontal line is by the characteristic time of the structure formation $t_c (= k_d/k_a)$. As the strength of shear flow increases, η_{ss} converges to the viscosity ratio $\xi = 0.00990$ (14) of completely-broken structure to full structure.

In Eq. (1), k_a [1/s] describes the rate of Brownian recovery and the destruction parameter k_d [-] is related to structure sensitivity to applied shear-rate. In this model, λ is restricted to $\lambda \in [0, 1]$; $\lambda = 0$ denotes completely broken state and $\lambda = 1$ represents fully recovered microstructure respectively.

Another equation of a structure-kinetics model is a constitutive equation. We consider a purely viscous (non-elastic) Moore fluid [13], in which the viscosity of a material depends on λ as

$$\eta(\lambda) = \eta_\infty + \eta_{str}\lambda. \quad (3)$$

Here, η_{str} expresses the structural contribution to the viscosity and η_∞ the residual viscosity when the microstructure is completely broken down ($\lambda = 0$). In the form (3), it is assumed that the high shear limiting behavior is expected to be Newtonian, ignoring inter-particle forces once the reversible floc structures have been destroyed completely [11]. From now on, we will simply call this combination of model Eq. (1) and Eq. (3) as a Moore thixotropy model. This relatively simple model has been employed for computer simulation and theoretical studies of thixotropic fluids [33, 36, 37]. It also has been adopted to model and predict real materials: thixotropy in blood [38] and drilling fluids [39].

The parameters $\{k_d, k_a, \eta_\infty, \eta_{str}\}$ of the Moore thixotropy model, Eq.(1) and Eq.(3), are usually calibrated from data (e.g., transient shear data) collected at simplest geometries from a rheometer [1]. The Moore model has a characteristic time of structure formation $t_c = k_d/k_a$. In a homogenous shear flow, where no gradient of λ exists in \mathbf{u} direction ($\mathbf{u} \cdot \nabla \lambda = 0$), the homogenous solution of material structure is determined by t_c as $\lambda_{ss} = 1/(t_c \dot{\gamma} + 1)$. Thus, the long term behavior of the Moore model at simple shear test can be found by substituting λ_{ss} to Eq. (3),

$$\eta_{ss}(\dot{\gamma}) = \eta_\infty + \frac{\eta_{str}}{t_c \dot{\gamma} + 1}. \quad (4)$$

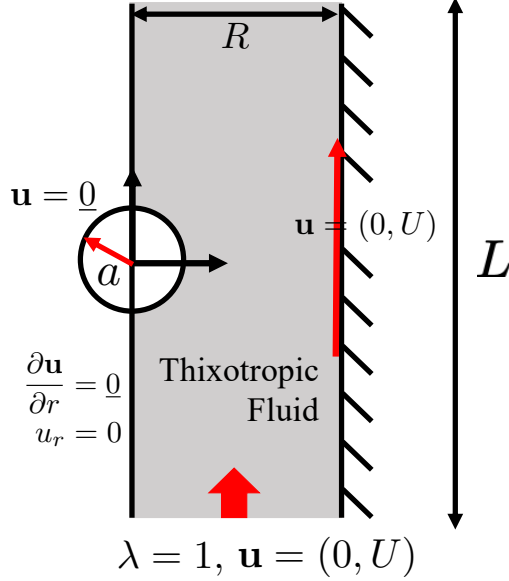


Figure 2: Schematic representation of a settling sphere inside a tube filled with a fluid. The boundary conditions for $\mathbf{u} = (u_r, u_z)$ are described on the frame of the sphere. The simulation domain for the axisymmetrically constrained case is shaded.

Figure 1 shows the steady state viscosity η_{ss} as a function of applied shear-rate $\dot{\gamma}$ in dimensionless scales. The viscosity is normalized by $\eta_\infty + \eta_{str}$ and the shear rate by t_c . The former is the normalized viscosity with respect to viscosity of fully structured material and the latter compares the flow strength to material time scale. Note that while there are infinite combinations of k_a and k_d to simultaneously fit steady shear data, t_c will remain as a constant.

2.2 Flow scenario

We consider a thixotropic flow (with density ρ_f) around a solid sphere settling under gravity g . The sphere has radius a and is falling at constant velocity U . As shown in the schematic Figure 2, the flow is confined by an infinitely long tube (radius R) filled with fully structured ($\lambda(\mathbf{x}) = 1$) thixotropic material. For many multi-particle systems (e.g., colloids and suspensions), viscous forces dominate the advective inertia forces, and thus inertia effects are not a practical concern [40]. Thus, we assume Stokes flow (or creeping flow), which characterizes a slow flow with high viscosity and small-length scale. (i.e. $Re \ll 1$).

The incompressible Stokes flow around a sphere is governed by momentum and mass conservations,

$$\nabla \cdot \boldsymbol{\tau} - \nabla p = 0, \quad (5)$$

$$\nabla \cdot \mathbf{u} = 0. \quad (6)$$

Here, $p = p^a + \rho_f g z$ is the modified pressure, which is the sum of ambient pressure p^a and hydrostatic pressure $\rho_f g z$. We assume the flow is axisymmetric. With a cylindrical coordinate, the flow around a 3-dimensional sphere in a cylindrical pipe reduces to 2-dimensional flow (u_r, u_z) , because $u_\theta = 0$ and $\partial/\partial\theta = 0$.

The steady state ($\partial/\partial t = 0$) structure-kinetics equation

$$(\mathbf{u} \cdot \nabla \lambda) + k_d \dot{\gamma}_s \lambda - k_a (1 - \lambda) = 0, \quad (7)$$

η_{str}	100.0 Pa·s
η_{∞}	1.0 Pa·s
k_a	0.1 s ⁻¹
k_d	1.0
t_c	10 s (= k_d/k_a)

Table 1: Thixotropic model parameters used in simulation

is coupled with the momentum conservation, in a way that the material stress $\boldsymbol{\tau}$ is described by the constitutive equation with Moore viscosity function (3)

$$\boldsymbol{\tau} = (\eta_{\infty} + \eta_{str}\lambda)\dot{\boldsymbol{\gamma}}. \quad (8)$$

The boundary conditions are described in the frame fixed at the center of the sphere,

$$u_z = U \quad \text{at} \quad r = R \quad \text{or} \quad z = \pm \frac{1}{2}L, \quad (9)$$

$$u_r = u_z = 0 \quad \text{at} \quad \sqrt{r^2 + z^2} = a. \quad (10)$$

with axisymmetric constraints,

$$u_r = 0 \quad \text{and} \quad \frac{\partial u_r}{\partial r} = 0 \quad \text{at} \quad r = 0. \quad (11)$$

In the current frame, the fully structured ($\lambda = 1$) material is being convected with velocity U from the bottom boundary (in-flow boundary). Thus, the boundary condition for Eq. (7) is

$$\lambda = 1 \quad \text{at} \quad z = -\frac{1}{2}L. \quad (12)$$

The aforementioned boundary conditions are summarized in the schematic Figure 2.

In this flow configuration, we define a quantity of interest as the resistance \mathcal{D} of the falling sphere, which can be calculated by the surface integral over the sphere surface ∂S ,

$$\mathcal{D} = \int_{\partial S} \mathbf{e}_z \cdot (-p\mathbf{I} + \boldsymbol{\tau}) \cdot \mathbf{n} dA, \quad (13)$$

where \mathbf{e}_z is the unit vector in z -direction, \mathbf{n} is the normal vector, and \mathbf{I} is the identity tensor.

2.3 Parameters and Dimensionless numbers

The flow problem is solved by a numerical solver, which will be introduced later in Sec 2.4. The numerical scheme has a set of input parameters $\{\eta_{\infty}, \eta_{str}, k_d, k_a; a, R, L, U\}$. Here, the first four parameters are the rheological model parameters and represent the intrinsic property of a material. The other four are flow-scenario parameters and denote the boundary condition or geometry. Model parameters and scenario parameters are independent; one may consider various flow scenarios for a single material at any time. Since the main goal of this paper is to illustrate how the material intrinsic thixotropy interplays with a non-homogenous flow, we first fix the model parameters as described in Table 1 in the subsequent analysis, unless otherwise stated.

The confining cylinder has radius $R = 0.1$ m. Ideally, we consider a sphere settling in infinitely long tube. However, it is impractical for the domain exterior L to extend out to infinity in simulations.

Therefore, the computational domain is cut off by large but finite length L_0 . The simulation domain has $L_0/R = 8$. It is confirmed that our numerical results do not change with the variation of this parameter. At first, the sphere radius is set as $a = 0.025$ m, and in Sec 4.3, the effect of confinement (a/R) will also be discussed separately.

Now, the model thixotropic fluid flow can be characterized by a few dimensionless numbers. First, the viscosity ratio ξ of completely-broken structure to full structure is

$$\xi = \frac{\eta_\infty}{\eta_\infty + \eta_{str}} = 0.00990. \quad (14)$$

We normalize the velocity of a falling sphere using t_c and the length scale a as

$$U^* = \frac{t_c U}{a} \quad (15)$$

U^* indicates external flow-strength compared to material timescale. In numerical simulations, we will investigate the effect of thixotropy at different time scale by changing U . This is equivalent to consider a range of different mass of sphere, because at steady state, a force balance yields

$$\mathcal{D}(U) = \frac{4}{3}\pi a^3(\rho_s - \rho_f)g, \quad (16)$$

where ρ_s is the density of a settling sphere. In experiment, it is often achieved through a “force-control” perspective, i.e. changing the density of a sphere and measuring the terminal velocity [41]. We also define the drag coefficient C_s of a thixotropic fluid as

$$C_s \equiv \frac{\mathcal{D}}{K6\pi(\eta_\infty + \eta_{str})aU}, \quad (17)$$

where \mathcal{D} is the resistance acting on the sphere and $K = K(a/R)$ is the wall correction factor given as a Faxen series for a/R [40]

$$K = \left[1.0 - 2.10444 \left(\frac{a}{R}\right) + 2.0877 \left(\frac{a}{R}\right)^3 - 0.94813 \left(\frac{a}{R}\right)^5 - 1.372 \left(\frac{a}{R}\right)^6 + 3.87 \left(\frac{a}{R}\right)^8 + 3.87 \left(\frac{a}{R}\right)^{10} \right]^{-1}. \quad (18)$$

The inclusion of K in the definition of C_s is useful to compare \mathcal{D} in thixotropy fluid to the existing Newtonian analytic solution, and hence to isolate the effect of thixotropy on resistance. For example, numerically calculated \mathcal{D} through the form (13) can be rewritten as $\mathcal{D} = K6\pi\eta^e U a$ by introducing an effective viscosity $\eta^e = \mathcal{D}/(K6\pi U a)$. In this case, η^e represents the gross viscosity acting on the sphere from the flow field and carries information on structural profile $\lambda(\mathbf{x})$ associated thixotropic behavior. Then, the form of C_s (17) is equivalent to the ratio of the effective viscosity η^e to the viscosity of fully-structured state $\eta_\infty + \eta_{str}$. Thus, C_s can be understood as a measure of viscosity relative to that of fully structured state. In addition, considering that the linear relation between η and λ in Eq. (3), C_s can also be understood to present the relative amount of preserved structure compared to full structure. In this work, the possible-minimum value of C_s is given as

$$C_{s\min} = \frac{\eta_\infty}{\eta_\infty + \eta_{str}} = \xi, \quad (19)$$

for the case where the sphere travels through the completely-broken structure.

ξ	$\frac{\eta_\infty}{\eta_\infty + \eta_{str}}$	The viscosity ratio of completely-broken structure to full structure
U^*	$\frac{t_a U}{a}$	Normalized falling velocity
Cs	$\frac{\mathcal{D}}{K6\pi(\eta_\infty + \eta_{str})a\bar{U}}$	Drag coefficient
k_d	-	Destruction parameter
a/R	-	Confinement Ratio

Table 2: Dimensionless numbers characterizing the model thixotropic fluid flow.

Lastly, we consider the effect of dimensionless model parameter k_d and ξ separately in Section 4.1 and 4.2. At given U^* , k_d determines the relative strength of shear-induced structure breakdown compared to structure convection effect. The list of dimensionless number is summarized in Table 2. It is useful to note that in the limit of either $\xi \rightarrow 1$, $U^* \rightarrow 0$, or $k_d \rightarrow 0$, the resistance (and flow solution) converges to that of a Newtonian fluid with the full-structured viscosity $\eta_\infty + \eta_{str}$ and thus $Cs \rightarrow 1$. In the other limit, $U^* \rightarrow \infty$ and $k_d \rightarrow \infty$, Cs will converge to Cs_{\min} .

2.4 Numerical Method

The governing equations (5) to (7) are solved numerically with finite-element method (FEM) using a C++ FEM software library `deal.II` [42, 43]. The primary variables are the two velocity components (u_r, u_z), pressure p , and structure parameter λ .

We linearize the set of governing equations by decoupling the structure kinetics equation (7) from the conservation equations. We take Picard iterations form (also known as fixed-point iteration), which is a simple and frequently used method for nonlinear problems. In this method, we compute the viscosity as a function of the previous structure parameter λ and solve for a new velocity and pressure field repeatedly. It is known that the choice of an initial solution is important to obtain a converging solution. We start from a Newtonian field with viscosity $\eta(\mathbf{x}) = \eta_\infty + \eta_{str}$ (i.e., $\lambda(\mathbf{x}) = 1$) and Picard iterations proceed: for each k step, the incompressible flow ($\mathbf{u}^{k+1}, p^{k+1}$) is solved with λ^k from the previous iteration

$$-\nabla p^{k+1} + \nabla \cdot \left[\eta(\lambda^k) \mathbf{u}^{k+1} \right] = 0, \quad (20)$$

$$\nabla \cdot \mathbf{u}^{k+1} = 0. \quad (21)$$

These equations represent a symmetric saddle point problem, and the function spaces should satisfy the Ladyzhenskaya-Babuska-Brezzi (LBB) condition. To satisfy this, we employ the second-order Taylor–Hood elements [44], composed of continuous piecewise quadratic element for \mathbf{u} and continuous piecewise linear for p . Schur complement approach is used for solving the linearized system for (\mathbf{u}, p) .

Once the flow solution (\mathbf{u}^{k+1}, p^k) is found, the scalar λ^{k+1} is updated according to

$$\mathbf{u}^{k+1} \cdot \nabla \lambda^{k+1} + k_d \dot{\gamma}_s \lambda^{k+1} - k_a (1 - \lambda^{k+1}) = 0. \quad (22)$$

As standard Galerkin method is numerically unstable for this advection type equation (22) discontinuous Galerkin (DG) approximation with degree 2 is used for $\lambda(\mathbf{x})$ [45, 46]. The advantages of using DG method is that it solves hyperbolic system using FEM without artificial viscosity for

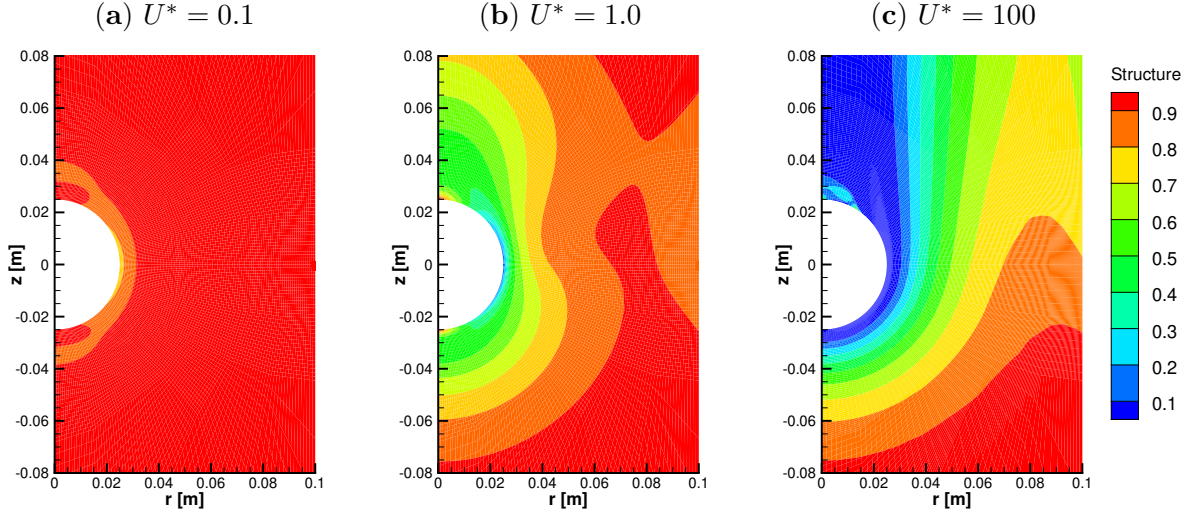


Figure 3: Structure $\lambda(\mathbf{x})$ at $U^* = 0.1, 1.0, 100$ at confinement ratio $a/R = 0.25$ $U^* = (t_c/a)U$ represents the ratio of thixotropic time scale to the flow strength. When $U^* = 0.1$, almost full structure is maintained and solution is close to Newtonian with viscosity $\eta_\infty + \eta_{\text{str}}$. As U^* increases, broken structures (blue region) start to appear from the vicinity of the sphere $(r, z) = (a, 0)$.

stabilization. In complex fluid flows simulation, the method has been often adopted for viscoelastic flows which has stress being convected in the domain [46].

The weak form for Eq. (22) is defined locally at each element K in domain Ω . To derive it, we multiply the test function w on both sides of Eq. (22) and take integral by part on the advection term,

$$\int_K [w(k_d \dot{\gamma}_s + k_a) \lambda^{k+1} + (\mathbf{u}^{k+1} \cdot \nabla w) \lambda^{k+1} - k_a w] dV + \int_{\partial K} [\mathbf{u} \cdot (w^+ \mathbf{n}^+ + w^- \mathbf{n}^-) \lambda^{k+1}] dS = 0. \quad (23)$$

Here, the superscripts denote the upwind (-) and downwind (+) values at the internal faces respectively. For numerical stability, we select upwind flux $(\lambda^{k+1})^-$ for face integrals. The boundary condition $(\lambda = 1)$ at the inlet replace the second integral term for faces located at $z = -L/2$. The bilinear form for Eq. (23) is solved by GMRES solver [47] with a preconditionner constructed by incomplete LU factorization [48].

A single simulation runs with 49,152-elements (mesh) resulting the number of degree of freedom for 395,010 for \mathbf{u} , 49,601 for p , and 196,608 for λ in total. The convergence criteria $\zeta = 10^{-8}$ used for Picard iteration is relative L_2 -norm difference of (u_r, u_z, p, λ) between subsequent k iteration. It is confirmed that our results do not change with the variation of ζ . To verify the present numerical scheme, we used the method of manufactured solution, whose procedure and result are summarized in Appendix A.

3 Thixotropy determined by interplay of three competing factors

Thixotropic behavior of a Moore fluid flow around the solid sphere is governed by the structural kinetic evolution of $\lambda(\mathbf{x})$. At steady state, $\lambda(\mathbf{x})$ solution is determined by Eq. (7), which consists of three factors: structure recovery by Brownian motion, shear-induced breakdown, and the convection of microstructure. Each factor has its own time scale. Firstly, the model parameter k_a [s⁻¹]

represents the time scale for Brownian structure recovery, which has nothing to do with the flow solution \mathbf{u} . Secondly, the time scale for shear-induced breakdown varies at each space due to its dependency on \mathbf{u} . Considering the characteristic shear-rate U/a of the flow, the breakdown timescale for overall domain is estimated as $(Uk_d)/a$ [s^{-1}]. It is worth noting that the normalized velocity (15) is the ratio of the time scale for shear-induced breakdown to that of structure recovery. Lastly, the time scale for the convection is related to U/a [s^{-1}] because the flow rate of convecting material is proportional to U and a sphere with smaller radius a is more easily enveloped by the same amount of convecting material. The time scale of both structure-convection and shear induced breakdown decreases in the same scale, when U is increased.

Figure 3 shows the structure profile at three different U^* (0.1, 1 and 100). When $U^* = 0.1$, the Brownian structure recovery, which has the shortest time scale, is dominant over the other two factors. Thus, $\lambda(\mathbf{x})$ remains homogenous in the flow field with almost full structure $\lambda \approx 1$. For example, $\lambda_{U^*=0.1}(\mathbf{x})$ shown in Figure 3(a) has just a little inhomogeneity just around the sphere. As U^* increases, the other two factors start to play an important role in determining $\lambda(\mathbf{x})$. The strengthened shear-induced structure breakdown effect is manifested by non-homogenous $\lambda_{U^*=1}(\mathbf{x})$ profile as shown in Figure 3(b). As U^* increases further, the effect of Brownian structure recovery becomes negligible compared to other two factors. When $U^* \gg 1$, the shear-induced breakdown effect and the convection of full microstructure reach an equilibrium, since both factors increase with the same scale to U^* . Consequently, a further increase in U^* does not cause remarkable change in $\lambda(\mathbf{x})$ profile. For instance, $\lambda(\mathbf{x})$ at $U^* = 200$ in Figure 4(a) and $U^* = 100$ in Figure 3(c) demonstrate barely any difference as displayed in Figure 4(b). Here, the minute difference at the wake of the sphere is attributed to the fact that fluid elements in this region are mostly subjected to extensional stress rather than shear stress; even a higher velocity U cannot lead enough shear to induce completely breakdown structure behind the sphere. Also, the fluid elements in this region are not replaced by the convecting structured material from the front of the sphere due to the no-slip condition on the sphere surface. Therefore, a Brownian recovery effect still plays a significant role even at larger U^* . The corresponding viscosity field reconstructed from $\lambda(\mathbf{x})$ is shown in Figure 4(c).

For more quantitative analysis on the three competing factors, the resistance of the sphere is investigated. The distribution profile of $\lambda(\mathbf{x})$ in Figure 3 takes a 2-dimensional form that prevents a more quantitative description and intuitive understanding of thixotropy in the current problem. Recognizing that the resistance \mathcal{D} , which can be calculated through the form (13), implicitly carries the information on $\lambda(\mathbf{x})$, we interpret that \mathcal{D} represents a measure of the distribution of $\lambda(\mathbf{x})$. The transition between three competing factors will therefore also be reflected in this single parameter. Figure 5(a) shows \mathcal{D} as a function of settling speed U . The scale of Reynolds number (Re) in Figure 5(a) varies, since we considered a wide range of settling velocity U . While Re is fully determined if the fluid density ρ_f is specified, our parametric study with respect to U actually implies that the density difference between the sphere and fluid is varied. For a rough estimations on $Re(=\rho_f U a / \eta)$, we first assume that $\rho_f \approx O(1000)$ kg/m³. Considering the sphere radius $a = 0.025$ m and thixotropic viscosity 100-15 Pa · s, we estimate the range of Re as 10^{-5} to 0.8. For a higher Re regime, flow solution may be significantly influenced by nonlinearity coming from inertial phases.

We also plot the relationship between the resistance coefficient Cs and U^* in Figure 5(b), which has a form of sigmoid shape with two asymptotes. The curves in Figure 5 are divided into three regime: Newtonian-fluid regime at $U^* \ll 1$, terminal regime at $U^* \gg 1$, and the transient regime in between. In the first regime marked with red circles, the thixotropic fluid behaves like a Newtonian fluid with viscosity $\eta_\infty + \eta_{str}$ as prescribed. In this regime, \mathcal{D} follows the analytic resistance solution of Newtonian, i.e., $\mathcal{D} = K6\pi(\eta_\infty + \eta_{str})Ua$. Likewise, the Cs in Figure 5(b) is maintained almost constant at 1, which implies that the thixotropic fluid is fully structured. As U^* increases, \mathcal{D} shows a sub-linear increase (i.e. $\mathcal{D} \propto U^n$, where $0 < n < 1$), which is manifested by green circles in the

middle of Figure 5(a). Accordingly, C_s starts to decrease and enters the transient regime, which is also marked with the same green circles in Figure 5(b). In terms of the explanation via the three competing factors, the transition of C_s value is the result of a shift in the equilibrium of competing factors to more broken structure. With a further increase in U^* , thixotropic fluid finally reaches the terminal regime, where a balance between the structure convection effect and the shear-induced breakdown is accomplished. As marked with blue circles, \mathcal{D} increases linearly again with respect to U in this regime. However, it should be noted that the flow is clearly distinguished from that of Newtonian flow, even though \mathcal{D} increases linearly with U . For example, the flow solution shown at $U^* = 200$ in Figure 6 has fore-aft asymmetry. This cannot be observed in Newtonian Stokes flow. This asymmetry is attributed to the effect of thixotropy. In the front of the sphere, the decreasing fluid viscosity induces a larger shear-rate and hence a greater pressure gradient. However, the fluid viscosity remains as a constant value η_{str} in the wake for the sphere as shown in Figure 4(c). This results in a relatively small gradient of pressure and velocity. The stronger positive pressure in the front of the sphere contributes to larger pressure drag. It is calculated that the pressure drag is nearly twice the viscous drag. It contrasts to Newtonian drag, the viscous part of which is twice the pressure part. It is also observed that u_z remains positive (upward) throughout the flow domain, indicating that there exists no negative-wake behind the sphere. It is conjectured that the fluid should be viscoelastic to generate negative wake [49, 50].

The origin of terminal regime is the result of dynamic equilibrium of shear-induced breakdown and the convection of structured fluid, which does not occur in Newtonian flow. The terminal regime at stronger flow-strength (large U^*) flows manifests as a new constant value in C_s - U^* curve. The C_s - U^* curve shown in Figure 5(b) looks qualitatively similar to the steady state viscosity curve of the Moore model flow in Figure 1. However, their mechanisms are different. In the case of the steady viscosity, the thixotropic model fluid structure can be completely broken at strong shear flow, because there is no structure-convection effect under homogenous flow condition as $\nabla\lambda = 0$. Therefore, the normalized steady state viscosity converges to the value of $\xi = 0.00990$. Yet, the terminal value of C_s is not equal to ξ . Rather, it converges to 0.15 that is almost 15 times larger than the pre-expected $C_{s\min} = \xi$. This is because the second plateau in C_s - U^* curve is a consequence of the compensation of structure breakdown by structure convection.

4 Effect of other dimensionless parameters

In the previous section, we focused on how $\lambda(\mathbf{x})$ changes depending on U^* with regards to equilibrium of three competing factors. In this procedure, we employed the drag coefficient C_s for a quantitative discussion on thixotropy in our model problem. In this section, we use the same framework to study the effect of other dimensionless numbers.

4.1 Destruction parameter

Here, we examine the effect of the destruction parameter k_d on microstructure profile $\lambda(\mathbf{x})$ and C_s of the sphere. Shown in Figure 7 is $\lambda(\mathbf{x})$ from additional simulations that are conducted with $k_d = 0.1$ and 8 at $U^* = 50$. The confinement ratio a/R remained the same as before. Herein, the boundary condition U (falling velocity) is modified accordingly to obtain the same U^* condition for thixotropic fluids with different k_d values. As k_d increases, fully broken structure (blue region) expands around the sphere. The increase in k_d shifts the balance, which determines the qualitative shape of $\lambda(\mathbf{x})$, toward more broken structure in the flow domain by intensifying the effect of shear-induced breakdown. C_s - U^* curves for 3 different k_d values are shown in Figure 8. The variations in the shape of $\lambda(\mathbf{x})$ is well-reflected in the C_s - U^* curve, the analysis of which enables

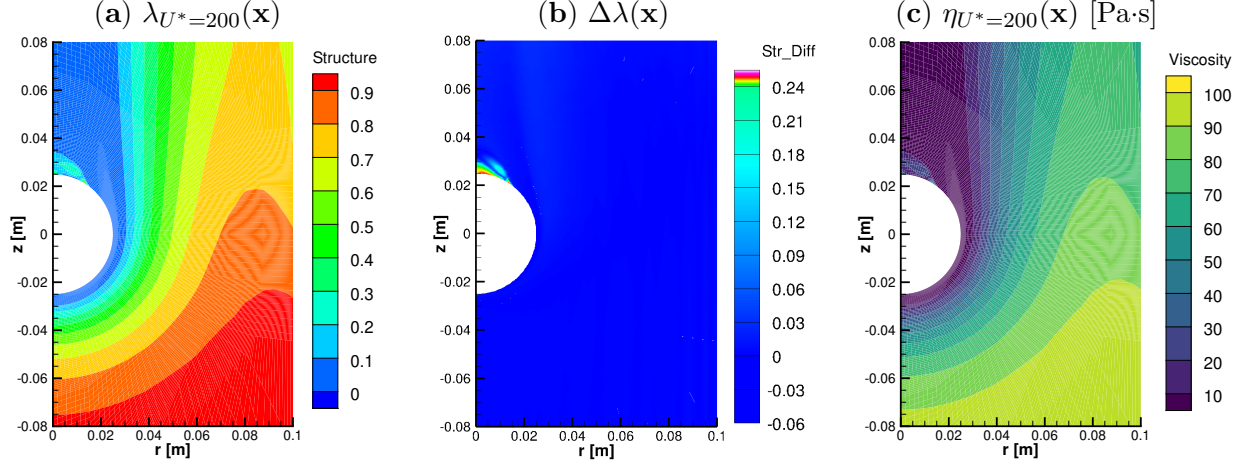


Figure 4: (a) $\lambda(\mathbf{x})$ at $U^* = 200$. (b) Difference in structure solution between $U^* = 200$ and $U^* = 100$. Due to structure convection, the solution shape of λ is maintained qualitatively similar to that of $U^* = 100$ in Figure 3c. (c) Corresponding viscosity field $\eta(\mathbf{x}) = \eta_\infty + \eta_{str}\lambda(\mathbf{x})$.

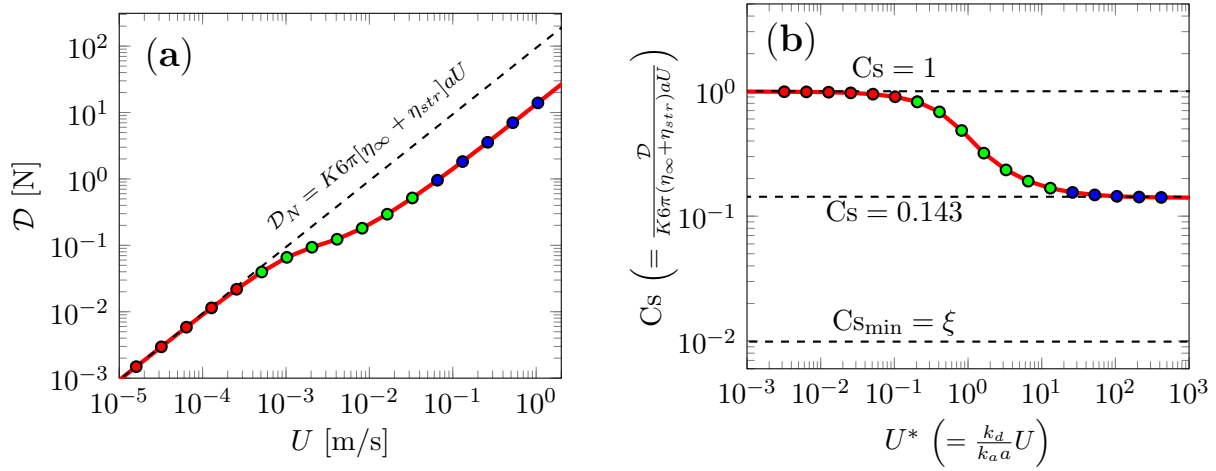


Figure 5: (a) Prediction of \mathcal{D} for various U . The dashed line is Newtonian resistance \mathcal{D}_N with viscosity $\eta_\infty + \eta_{str}$. (b) The relation between C_s and U^* . The vertical line represents gross viscosity (normalized by $\eta_\infty + \eta_0$) that the sphere experiences by the viscosity field $\eta(\mathbf{x})$. The shape of the C_s - U^* curve is qualitatively similar to the flow curve (Figure 1). The C_s value at the terminal regime (blue points) does not equal to ξ due to the structure convection.

more quantitative explanation of the balance shift induced from the increase in k_d . At small U^* , there exists no remarkable difference in C_s , which is attributed to the fact that thixotropic behavior in this regime is dominated by Brownian structure recovery. As U^* increases, the shear-induced breakdown and the convection become the two dominating factors that determine C_s . At large U^* , the larger k_d results the lower C_s in the terminal regime, indicating that the balance between breakdown and convection is achieved when the structure is more broken.

Comparison of thixotropic fluid with Generalized Newtonian Fluid (GNF), which takes a form of $\tau = \tau(\dot{\gamma})$, provides a useful insight on the role of destruction parameter k_d . The brown curve

with square symbol in Figure 8 represents the Cs- U^* curve of Cross model [51]

$$\boldsymbol{\tau}_{\text{cross}}(\dot{\gamma}_s) = \eta_{\text{cross}}(\dot{\gamma}_s)\dot{\gamma} = \left[\eta_{\infty} + \frac{\eta_{\text{str}}}{1 + (k_c \dot{\gamma})^n} \right] \dot{\gamma}. \quad (24)$$

Cross fluid has been often compared to the Moore thixotropy model [10, 52], since it has the same steady-state viscosity η_{ss} at simple shear flow if $n = 1$, and $k_c = t_c (= k_d/k_a)$. For a Cross fluid, we characterize the flow strength U^*

$$U_{\text{cross}}^* = \frac{k_c U}{a}. \quad (25)$$

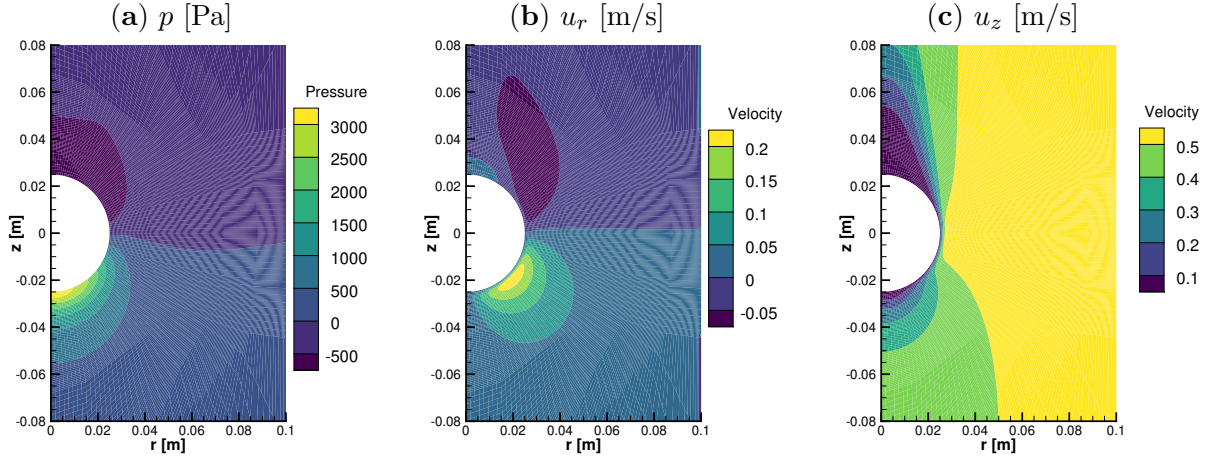


Figure 6: Flow solution (p, u_r, u_z) at $U^* = 200$. The flow solution has fore-aft asymmetric due to inhomogeneous viscosity field around the sphere.

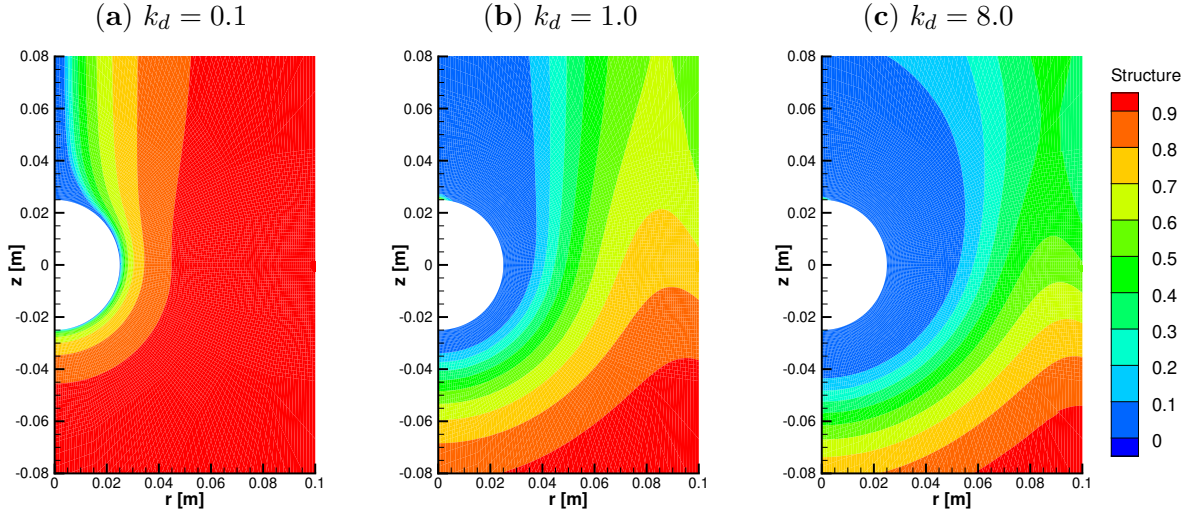


Figure 7: The shape of $\lambda(\mathbf{x})$ -solution with respect to k_d at $U^* = 50$. k_d determines the equilibrium between the shear-induced breakdown and the structure convection for large U^* values. As k_d increases, the fully broken structure (blue region) around the sphere expands to far field.

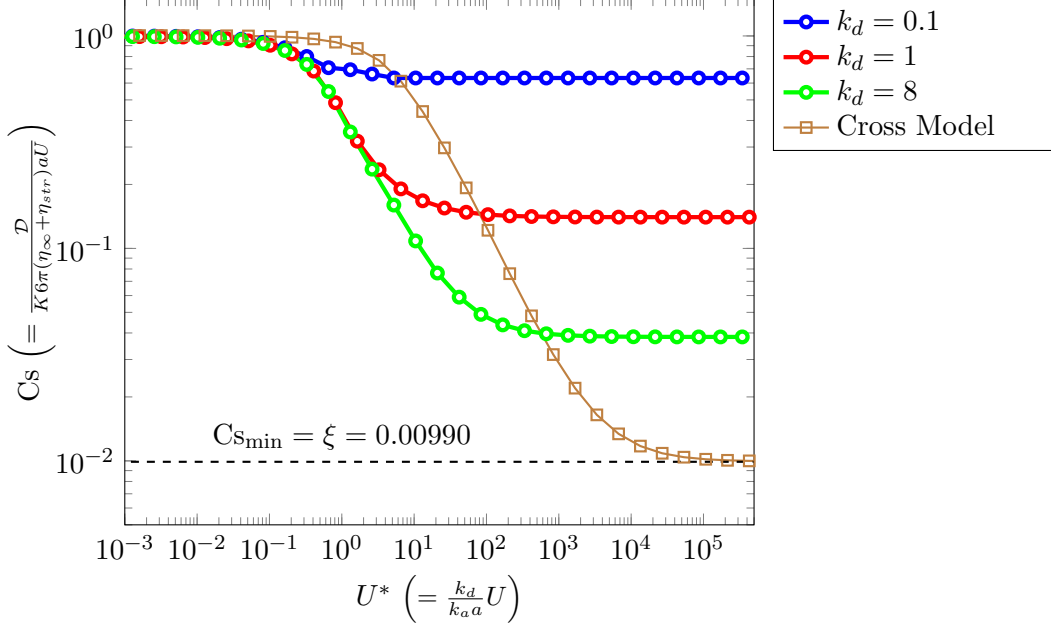


Figure 8: The effect of the destruction parameter k_d on the resistance. As k_d increases, fully broken region expands around the sphere and hence η_e decreases. A finite value of k_d distinguishes Moore thixotropy model from Generalized Newtonian model for $U^* \gg 1$.

The numerical scheme used for Cross fluid simulation is similar to the current numerical scheme. In this case, we do not need to consider the structure-kinetics equation, and Picard iterations proceed as follow,

$$-\nabla p^{k+1} + \nabla \cdot \left[\eta_{\text{cross}}(\dot{\gamma}_s^k) \mathbf{u}^{k+1} \right] = 0, \quad (26)$$

$$\nabla \cdot \mathbf{u}^{k+1} = 0. \quad (27)$$

More details on numerical procedures for GNF fluid are available elsewhere [53]. The Cs of Cross fluid at the terminal regime $U^* \gg 1$ is found as $Cs_{\text{min}} = 0.00990$. This can be accounted for the absence of convection effect in Cross fluid; GNF model assumes that the fluid rheology immediately responses to applied shear field and thus the convection is ignored. Consequently, fluid elements at large U^* exist with fully broken state $\lambda \approx 0$ and viscosity $\eta(\mathbf{x})$ over all domain can converge to η_∞ .

It is worth noting that the Cs of thixotropic fluid at large U^* converges to that of Cross fluid as k_d increases. This is because the increase in k_d induces fluid elements to respond more instantly to the applied shear-field. Therefore, when $k_d \rightarrow \infty$, the convection effect becomes insignificant in thixotropic fluid as in Cross fluid, which is intrinsically lacking the convection. This causes Cross fluid-like behavior of thixotropic fluid for large k_d .

4.2 The viscosity ratio

In this section, we focus on the effect of the viscosity ratio ξ . The analogy between the purely-viscous Moore thixotropy model and Generalized Newtonian model naturally extends to a discussion on the capability of the Moore thixotropy model for a thixo-viscoplastic materials. Ideally, the effective viscosity of an viscoplastic fluid is an infinite value. For example, the viscosity η_B of

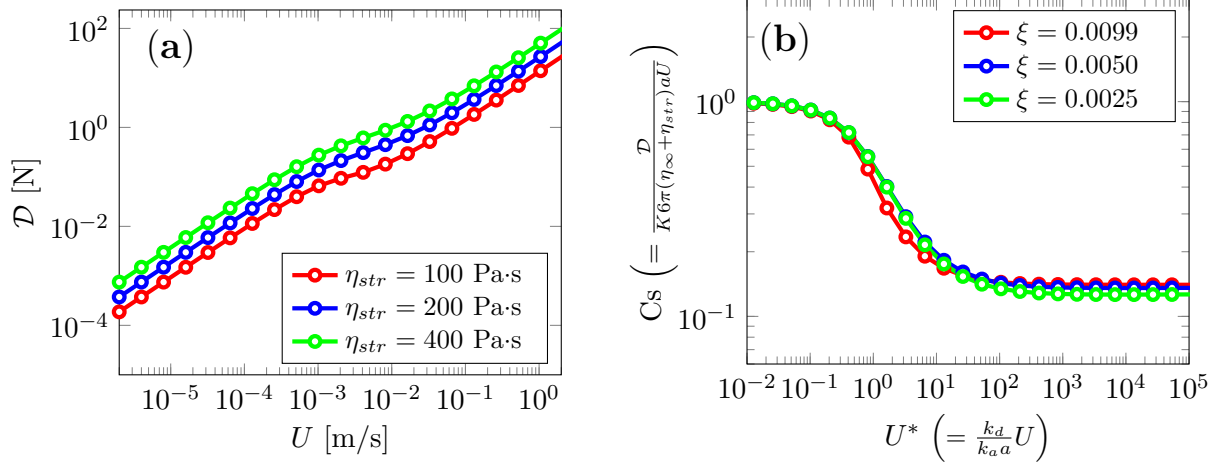


Figure 9: The effect of the structural viscosity η_{str} on (a) \mathcal{D} - U curve and corresponding (b) C_s - U^* . The increase in η_{str} shifts the \mathcal{D} - U curve upward, whereas \mathcal{D} - U remains relatively same because of the normalization factor $(\eta_\infty + \eta_{str})$ in the definition of C_s . In (a), it is shown that even at lower ξ values the transition from full structure viscosity to lower viscosity after a critical shear-rate still remains gradual in the current linear thixotropic model.

Bingham plastic fluid with two model parameter τ_y and η_∞ ,

$$\eta_B = \frac{\tau_y}{\dot{\gamma}_s} + \eta_\infty. \quad (28)$$

diverges to infinity in the limit of $\dot{\gamma}_s \rightarrow 0$. In numerical investigations, however, the non-elastic 3D versions of simple yield stress models are often employed with a regularized finite-value of viscosity [54, 55]. In case of Moore thixotropy, this corresponds to a case where η_{str} is far larger than η_∞ (thus, $\xi \rightarrow 0$). Given the similarity, for low values of ξ , it can be conjectured that the the current pure-viscous thixotropic model can achieve what simple viscoplastic models predict.

Additional simulations are conducted with different ($\eta_{str}=200, 400$ Pa·s) values, while other model parameters are fixed as given in Table 1. These cases correspond to $\xi=0.0050$ and 0.0025 . Figure 9 summarizes the results both in \mathcal{D} - U and C_s - U^* forms. As seen in Figure 9, the C_s - U^* curves remain relatively same due to the normalization factor $(\eta_\infty + \eta_{str})$ in the definition of C_s . When it comes to the \mathcal{D} - U curve, the increase in η_{str} shifts the curve upward due to the effect of increased viscosity around the sphere. Yet, even at lower ξ values, the transition from fully structured viscosity to lower viscosity after a critical shear-rate still remains gradual. This is contrast to what typical regularized viscoplastic models predict; in these models, a dramatic viscosity drop after a critical shear-rate manifests as a plateau in \mathcal{D} - U curve [53]. This is owing to the viscosity regularization terms, which are intentionally designed to mimic yielding processes. It is conjectured that the current linear model form, either structure-kinetics (1) or viscosity (3), should be modified to have exponential dependence on λ [56, 57] in order to achieve what simple viscoplastic model predicts. Yet, this extension shares the same underlying assumption that the materials exhibits no elasticity. In addition, this naive approach is fundamentally limited when it comes to predicting the important issue of the presence of anisotropic yield stress [58]. The interested reader on this issues is referred to additional reference where rheological models consider elastic and thixotropic response to a combination of shear and extensional deformations [50, 59] and computational implementation of these models in real flow scenarios [23, 60].

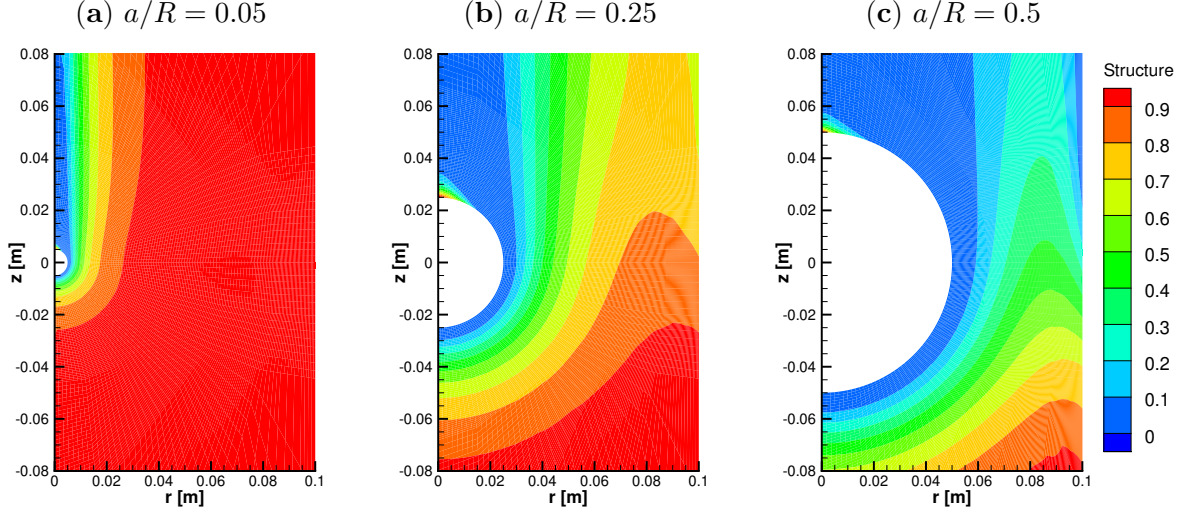


Figure 10: Solutions of structure λ for different confinement ratio a/R at fixed $U^* = 50$. As a/R increases, the balance between shear-break and the structure convection is achieved with more broken structures in the vicinity of sphere. When $a/R = 0.5$, the wall interaction starts to appear with the broken structures near the side wall.

4.3 Confinement effect

Geometry is another important factor that significantly contributes to a non-homogeneous flow of thixotropic fluid. In this section, we study how a geometrical factor modifies the competition of the three factors. Provided that the length of confining cylinder L is sufficiently large enough, the geometrical condition of the our model problem is uniquely characterized by the confinement ratio a/R . Accordingly, additional simulations are conducted with $a/R = 0.05, 0.25$ and 0.5 , while other model parameters are fixed as given in Table 1. Again, the falling velocity U is modified to obtain the same U^* condition. Shown in Figure 10 is the structure profile $\lambda(\mathbf{x})$ observed in three different geometry at $U^* = 50$. The value is located in the end of the transient regime in Figure 5(b). It shows significant difference in $\lambda(\mathbf{x})$ at different a/R values. In the case of the small sphere ($a/R = 0.05$), the bulk of fluid elements passes through the large area between the sphere and wall and thus the fluid is relatively less sheared compared to the large sphere case. Thus, shear-induced breakdown becomes insignificant whereas the convecting fresh full-structured elements easily refill the space around the sphere. As a result, the thixotropic fluid sustains a structured state as shown in Figure 10(a). On the contrary, if a/R increases, the thixotropic fluids elements become highly sheared, passing through a narrower area between sphere and wall. This makes the shear-induced breakdown predominant over refilling of fresh element. Consequently, the balance between shear-induced breakdown and the convection is achieved at more broken structure as shown in Figure 10(c).

The aspect of $\lambda(\mathbf{x})$ transition with respect to a/R variation is reflected in $Cs-U^*$ curve in Figure 11 as well. Here, we remind that our definition of Cs (17) takes into account the wall interaction factor, extracting the effect of thixotropy effect on resistance. The overall trend of three curves in Figure 11 is similar; they are all characterized by a sigmoid shape with two horizontal asymptotes. At large a/R , however, Cs drops much faster toward a lower plateau. The bigger and faster drop of Cs with respect to the increase in U^* is correlated to the balance achieved at more broken structure due to predominant shear-induced breakdown.

Considering how the variation of a/R affects both the transient regime of $Cs-U^*$ curve and

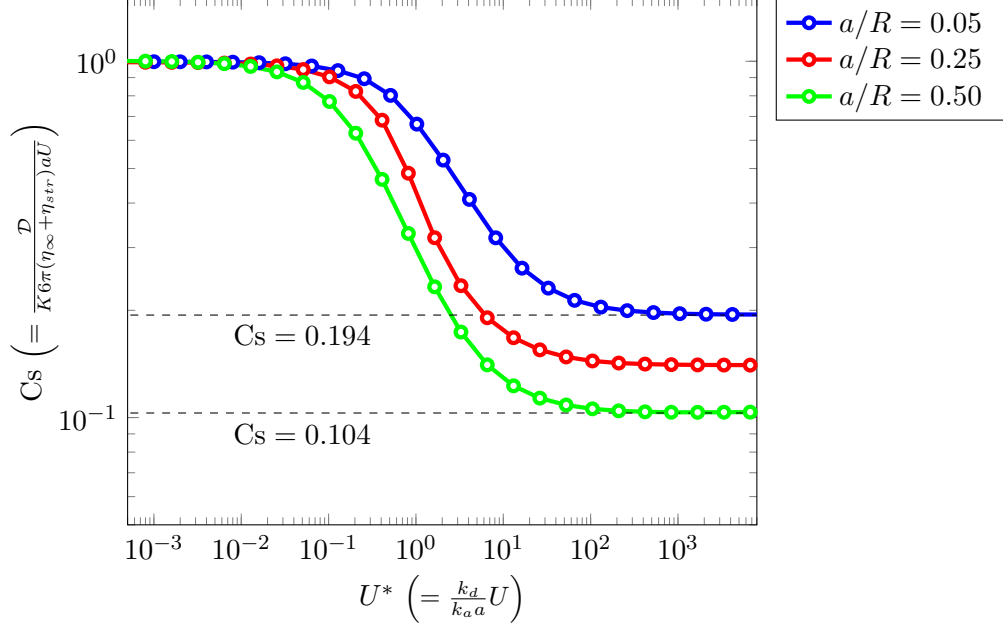


Figure 11: The variation of Cs - U^* curve at different confinement ratio (a/R). The effect of confinement is negligible at small U^* . At larger a/R , Cs drops much faster to lower plateau as U^* increases. Such effect is not confined to the terminal regime but greatly changes the shape of the transient regime, contrast to the effect of the destruction parameter k_d .

the terminal regime, the geometrical factor distinguishes itself from the destruction parameter k_d , the effect of which is mostly limited to the terminal regime. This suggests that a behavior of thixotropic fluid is not a sole result of the intrinsic material property, but that of involved interplay between intrinsic property and extrinsic geometrical factors of a flow. The implication is that one can accomplish a desired flow condition by the tuning flow geometry, which can be often easier than modifying the intrinsic property of a material.

5 Nonlinear thixotropic models

In this section, we examine how an addition of nonlinearity to the Moore thixotropy affects the non-homogenous flow. Although the Moore thixotropy model has been considered as a simple but effective model for various kinds of thixotropic fluids, it is sometimes inadequate to correctly describe a more complicated thixotropic behavior. Recent thixotropic modeling works aim to incorporate them by replacing explicit model-form with an implicit form [61, 62].

Within the purely-viscous thixotropic model context, a variety of modifications of Moore thixotropic model have also been employed for a more accurate description of sophisticated thixotropic behavior [1, 11]. The general modification is to include nonlinearity by considering high-order polynomial terms to either the constitutive equation

$$\tau(\lambda) = \eta_\infty \dot{\gamma} + (\eta_{str,1} \lambda + \eta_{str,2} \lambda^2 + \dots) \dot{\gamma}, \quad (29)$$

or the structure kinetic equation,

$$\frac{d\lambda}{dt} = (k_{a,1}[1 - \lambda] + k_{a,2}[1 - \lambda]^2 + \dots) - (k_{d1} \dot{\gamma}_s \lambda + k_{d2} \dot{\gamma}_s^2 \lambda^2 + \dots). \quad (30)$$

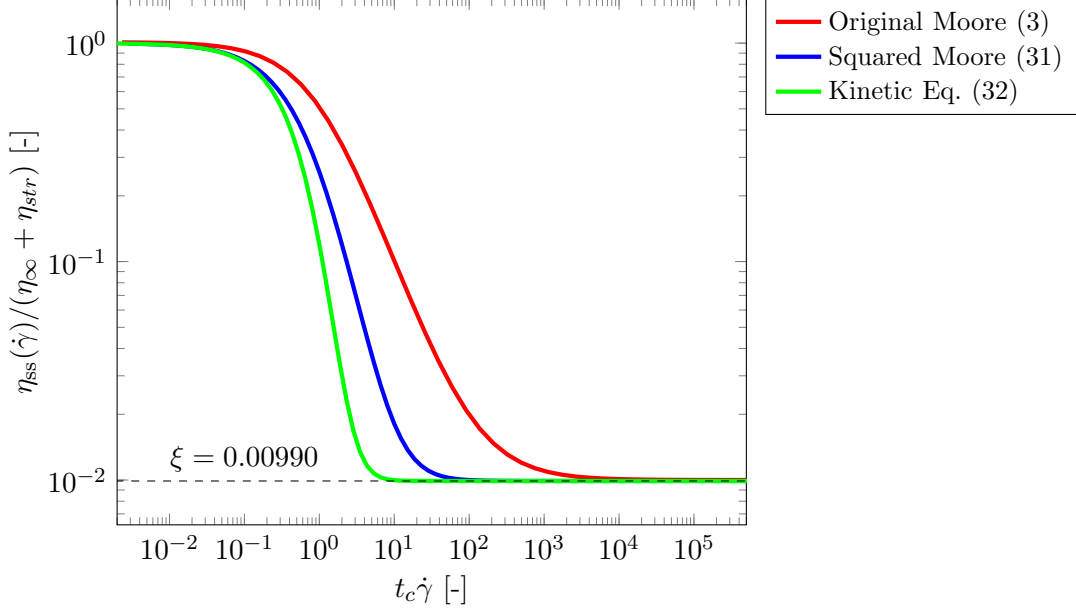


Figure 12: Steady shear viscosity η_{ss} of nonlinear thixotropic model considered in Section 5. The k_{d2} in structure-kinetics Eq. (32) is set as 1.0 [s], while the remaining model parameters are as in Table 1. The structural sensitivity to the applied shear-rate (32) is more significant than the sensitivity of the viscosity to microstructural change (31).

Because the additional high-order terms provide more degree of freedom to fit steady-shear and transient shear data simultaneously, these forms have been adopted for modeling slurry fuels [63, 64] and semisolid metal suspensions [65]. These additional material parameters cannot be directly related to the micromechanics of real material; the structure-kinetic method is phenomenological modeling in nature [11, 62]. In general, the use of extra high order terms should be penalized, unless they are legitimately supported from existing rheological data [66, 67]. Thus, we investigate two simple cases where nonlinearity is implemented by an addition of a second-order term respect to λ or $\dot{\gamma}_s$. It should be noted that these modified model forms are still purely viscous fluid and only consider shear-dependent rheology.

Firstly, we consider a nonlinearity in viscosity function

$$\eta(\lambda) = \eta_\infty + \eta_{str}\lambda^2. \quad (31)$$

instead of Eq. (3). The other governing equations, including the structure-kinetics equation, remain the same. The steady state shear viscosity η_{ss} of the viscosity model Eq. (31) is shown with the blue curve in Figure 12. It indicates that the viscosity of a material with extra higher order terms is more sensitive to microstructural change than the original is. In Figure 13(a), the resistance \mathcal{D} of a settling sphere in this model fluid is compared with that of the Moore viscosity. Here, the material parameters $\{\eta_\infty, \eta_{str}, k_d, k_a\}$ of both models are the same as those summarized in Table 1. Based on this result, Cs- U^* curves of the original Moore model and the nonlinear viscosity function (square term) are compared in Figure 13(b). As U^* increases, the Cs value of the new viscosity model shows a faster and larger drop because of the higher viscosity-sensitivity to structural breakdown (or decrease in λ). Yet, the terminal Cs value (0.095) results in the squared model (31) is still nearly 10 times larger than Cs_{\min} . This is because the results in the nonlinear viscous model are still governed by the balance between the structural breakdown and the structure convection.

Next, we focus on another modification of the Moore model where nonlinearity is introduced by

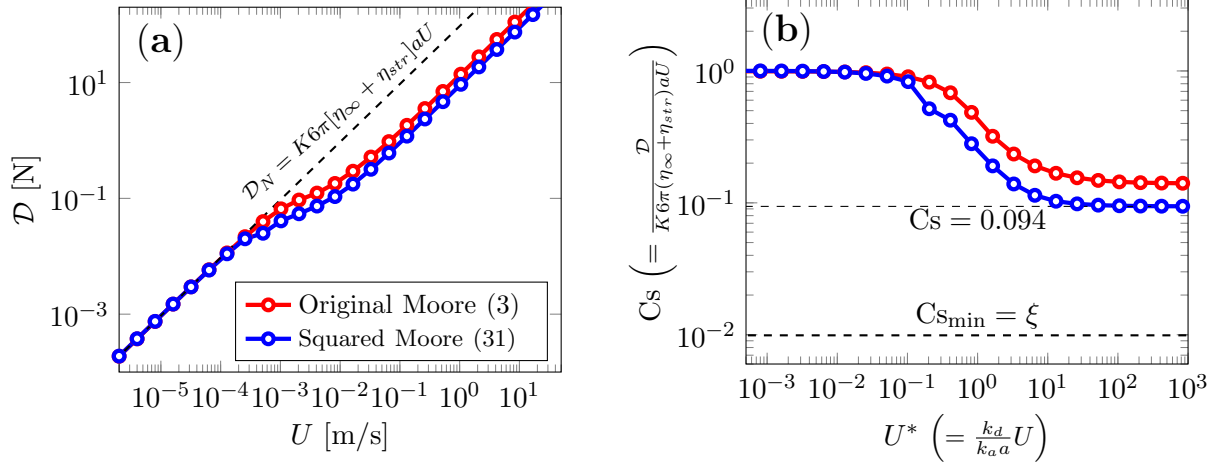


Figure 13: The effect of the modified viscosity function (31) on the (a) \mathcal{D} - U curve and (b) C_s - U^* curve is plotted. The nonlinearity implemented in the viscosity function (31) is still governed by the balance between structure breakdown and convection at large U^* .

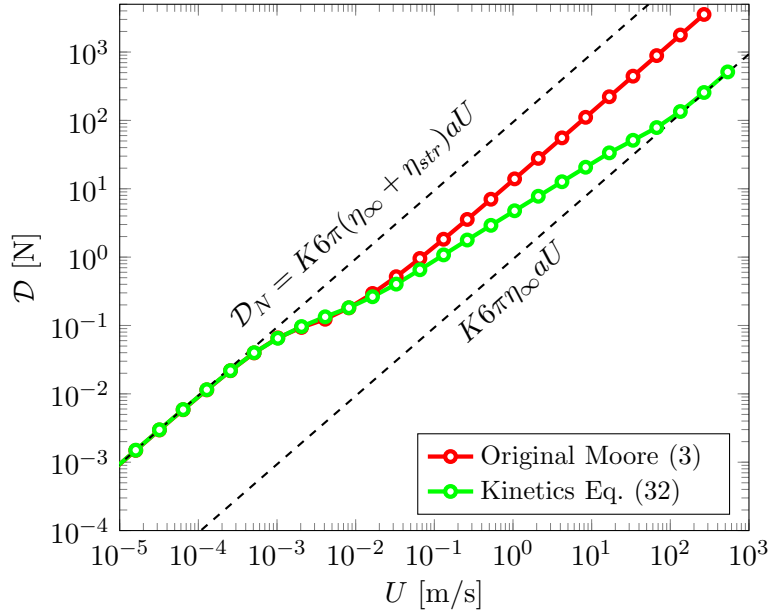


Figure 14: The resistance prediction for the nonlinear structure-kinetics equation (32). When the structure is more sensitive to applied shear rate than a linear scale, shear-induced breakdown effect dominates the Brownian recovery and structure convection as U^* increases. Therefore, \mathcal{D} converges to Newtonian resistance with viscosity η_∞ .

the addition of a square term to the structure-kinetics equation. In this case, the kinetics equation is given as

$$\frac{d\lambda}{dt} = \frac{\partial\lambda}{\partial t} + (\mathbf{u} \cdot \nabla\lambda) = -k_{d1}\dot{\gamma}_s\lambda - k_{d2}\dot{\gamma}_s^2\lambda + k_a(1 - \lambda), \quad (32)$$

instead of Eq. (1), while the constitutive equation is same as the original Eq. (3). In Figure 12, the steady state shear viscosity η_{ss} of the structure-kinetics model (1) is shown with the green curve in Figure 12. In this case, the homogenous structure solution in a simple shear flow changes to $\lambda_{ss} = 1/(t_c\dot{\gamma} + (k_{d2}/k_a)\dot{\gamma}^2 + 1)$ the structural change is more sensitive to the applied shear-rate. As

shown in Figure 12, The structural sensitivity to the applied shear-rate is more significant than the sensitivity of viscosity to microstructural change. In Figure 14, the resistance \mathcal{D} calculated from the original Moore model and the model with nonlinear structural kinetic equation (32) are compared. In both cases, material parameters $\{\eta_\infty, \eta_{str}, k_{d1} = k_d, k_a\}$ are given to match values in Table 1 and the new parameter k_{d2} in this nonlinear model is set as 1.0 [s]. Here, we report the simulation result with units (i.e., \mathcal{D} - U curve), because the strength of shear-induced breakdown from the kinetic equation (32) is much stronger than that of our previous definition of U^* (15); while breakdown effect is mostly governed by the second-order term $k_{d2}\dot{\gamma}_s^2$ when $U^* > 1$, we cannot compare these effect in the same scale because of the absence of the term in the original Moore model. As expected from steady shear viscosity (Figure 12), the Moore model with nonlinear structure-kinetic equation shows a faster transition in \mathcal{D} - U^* curve compared to the previous case with nonlinearity viscosity function. It also shows a more notable difference in that \mathcal{D} finally converges to that of Newtonian fluid with viscosity η_∞ as $U \rightarrow \infty$. This is because the strengthened breakdown effect becomes completely dominant over other two factors, and thus the structure convection cannot compensate the breakdown effect as $U^* \rightarrow \infty$.

In summary, adding nonlinearities in either in the viscosity function and the structure kinetic equation work differently. Thus, when nonlinear thixotropic models are considered, one should carefully distinguish whether the constitutive equation or the structural change equation is more sensitive upon consideration of relevant experimental measurement or designing flow process.

6 Conclusion

In this work, a non-homogenous flow of a Moore thixotropic fluid is explored in terms of an interplay between intrinsic thixotropy of materials and geometry of flow. As an example, the steady thixotropic flow around a settling sphere is analyzed by a numerical simulation. Combined with a typical Stokes flow solver, we employed an Discontinuous Galerkin approximation for advection-type structure-kinetics equation. The structure profile $\lambda(\mathbf{x})$ in the flow is quantitatively characterized by the resistance coefficient C_s and classified into three different regimes according to the normalized velocity U^* . This transition is discussed with regards to the balance of three competing factors: Brownian structure recovery, shear-induced structure breakdown, and the structure convection. At small U^* , thixotropic effect is negligible and Newtonian-like behavior is observed, since the overall dynamic is overwhelmed by the Brownian structure recovery. As U^* increases, the shear-induced breakdown and the convection become significant and the equilibrium of three factors shifts toward more structure-broken state. At large U^* , the final balance between breakdown and the convection is achieved, since both effects are proportional to U^* . Based on our findings, the effects of a destruction parameter and confinement are discussed. The destruction parameter k_d determines the the shape of the structure solution around the sphere for large enough U^* . It has been also shown that a finite value of k_d distinguishes a thixotropic model fluid from a Generalized Newtonian model in a non-homogenous flow. Moreover, the analysis on confinement effect emphasized the importance of geometrical factors in a material process with thixotropy. Finally, we investigated how two different ways of implementing nonlinearity in Moore model lead to different descriptions of thixotropic behavior.

Most of previous experimental and theoretical studies have focused on intrinsic properties of material itself, and thus assumed a homogeneous flow to provide effective modeling approaches for thixotropic behavior. By contrast, the current work distinguishes itself from the existing studies as it extends a scope to illustrating a complex interplay between the intrinsic thixotropy of materials and flow geometry. A near future work may include typical intricate examples: particles with

non-spherical shape (e.g, oblates [68], cylinders [69], cubes [70]), surrounding fluids with unsteady motion [71, 72], or motion of bubbles [73]. Understanding these problems will pave a way to realistic engineering of thixotropic fluid in practical application scenarios, e.g. establishing an effective flow-assurance strategy to ensure continuous flow of production crude oils and other industrial products [74, 75].

We close by recognizing the unresolved fundamental issues of a non-homogenous flow of complex fluids around a solid sphere [76, 77]. Most of materials show more complex rheological characteristics such as non-trivial extensional rheology, yield stress, and TEVP features [77, 78]. Therefore, understanding non-homogenous flow of complex fluid, which is conjectured to be a result of an interplay between intricate material rheology and flow geometry, is required for accurate design and control of practical fluid processes. Although a purely viscous thixotropic model is considered in this paper, our result is meaningful as an initial step to unravel the longstanding question of non-homogenous flows of complex fluids.

7 Acknowledgements

This research did not receive any specific grant from funding agencies in the public, commercial, or non-for-profit sectors.

Appendix A Code verification

To verify the numerical scheme used in this work, the order of accuracy and convergence are tested. Because the exact solution of the set of governing equations (5) to (7) is unknown, the method of manufactured solution is considered [79, 80]. In this framework, a selected ‘manufactured solution’ ($\tilde{\mathbf{u}}, \tilde{p}, \tilde{\lambda}$) is forced to be the exact solution by modifying the source terms, which are the right hand side of (5), (6), and (7). For example, we selected our manufactured solution as the Newtonian analytic solution of a flow around sphere falling with velocity U at infinite space [40],

$$\tilde{u}_{r_s} = U \cos \theta \left(1 + \frac{1}{2} \frac{a^3}{r_s^3} - \frac{3}{2} \frac{a}{r_s} \right), \quad (\text{A.1})$$

$$\tilde{u}_{\theta} = U \cos \theta \left(1 - \frac{1}{4} \frac{a^3}{r_s^3} - \frac{3}{4} \frac{a}{r_s} \right), \quad (\text{A.2})$$

$$\tilde{p} = \frac{3}{2} a U \left(\frac{\cos \theta}{r_s^2} \right), \quad (\text{A.3})$$

where r_s and θ are the radial distance and the polar angle of a spherical coordinate system with the origin at the center of the sphere. For $\lambda(\mathbf{x})$, the manufactured solution arbitrarily constructed by

$$\tilde{\lambda} = r_s \theta. \quad (\text{A.4})$$

In some part of the computational domain Ω , the constructed form $\tilde{\lambda}$ (A.4) exceeds $\lambda > 1$, which the model-form does not allow. Yet, there is no requirement for physical realism in the manufactured solution for the current purpose [81]. The form (A.4) is suitable to test all terms in the set of governing equations and simple enough to determine the analytic form of the corresponding source terms.

During the code verification stage, we assumed the simplest parameter values $\eta_{\infty} = \eta_s = 1$ Pa·s of the Moore viscosity function (3). To find the analytic expression for the corresponding source

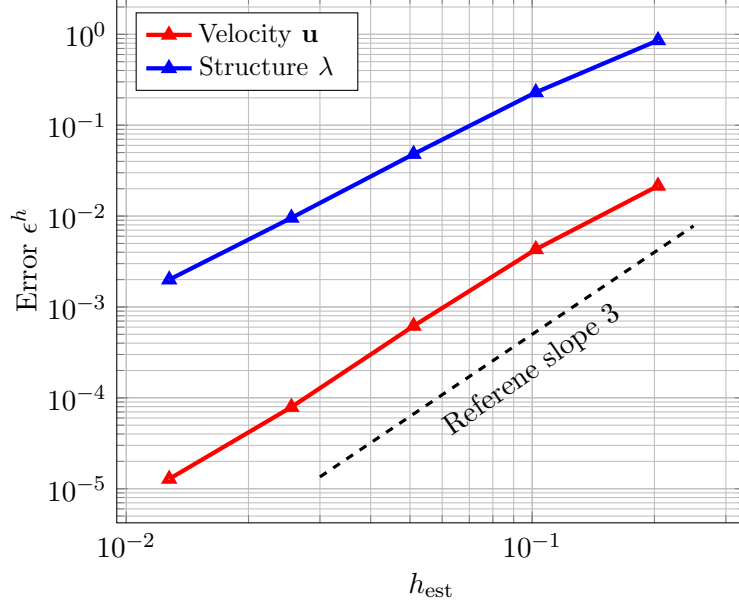


Figure A.1: Convergence of numerical solution (\mathbf{u}^h, λ^h) compared with manufactured analytic solution ($\tilde{\mathbf{u}}, \tilde{\lambda}$). At each discretization with N -elements, the L_2 -norm errors are plotted in log-log scale with the estimated cell average diameter $h_{\text{est}} = 1/\sqrt{N}$. Both numerical solution \mathbf{u}^h, λ^h converges to the exact solution at 3rd order.

terms in the momentum conservation $\vec{F} = (F_{r_s}, F_\theta)$, we first substituted (A.4) into the constitutive equation (8) to evaluate the material stress $\boldsymbol{\tau}$. After, resubstituting the resulted analytic form of stress $\boldsymbol{\tau}$ into the conservation of momentum (5), we obtained

$$F_{r_s}(r_s, \theta) = \frac{aU[(3a^2\theta - 6\theta r_s^2)\cos\theta + \frac{3}{2}a^2\sin\theta]}{r_s^4}, \quad (\text{A.5})$$

$$F_\theta(r_s, \theta) = \frac{aU[\frac{3}{2}(r_s^2 - a^2)\cos\theta + \frac{3}{2}\theta(a^2 - r_s^2)\sin\theta]}{r_s^4}. \quad (\text{A.6})$$

The source term of the mass conservation remains zero as our choice of $\tilde{\mathbf{u}}$ automatically satisfies the incompressible constraints, i.e. $\nabla \cdot \tilde{\mathbf{u}} = 0$. Similarly, substituting (A.1), (A.2) and (A.4) into the kinematic equation (7), we found the corresponding source term Q of structure-kinetics equation as

$$Q = \frac{3}{2}k_d\theta r_s aU^2 \sqrt{\frac{3\cos^2\theta(r^2 - a^2)^2 + a^4\sin^2\phi}{r^8}} + k_a\theta r_s + U\sin\phi \left(\frac{a^3U}{4r_s^3} + \frac{3aU}{4r_s} - 1 \right) + \theta U\cos\theta \left(\frac{a^3U}{2r_s^3} - \frac{3RU}{2r_s} + 1 \right). \quad (\text{A.7})$$

Finally, the numerical scheme described in Section 2.4 was used to solve the set of governing equation

$$\nabla \cdot \boldsymbol{\tau} - \nabla p = \vec{F}, \quad (\text{A.8})$$

$$\nabla \cdot \mathbf{u} = 0, \quad (\text{A.9})$$

$$(\mathbf{u} \cdot \nabla \lambda) + k_d \dot{\gamma}_s \lambda - k_a(1 - \lambda) = Q, \quad (\text{A.10})$$

and the order of accuracy is tested by comparing numerical solution $(\mathbf{u}^h, \lambda^h)$ to $(\tilde{\mathbf{u}}, \tilde{\lambda})$ at different number of discretizations. The scheme errors ϵ^h at each discretization are evaluated by the L_2 -norm difference between $(\mathbf{u}^h, \lambda^h)$ and $(\tilde{\mathbf{u}}, \tilde{\lambda})$. In Figure A.1, ϵ^h is plotted in log-log scale together with respect to $h_{\text{est}} = 1/\sqrt{N}$. Here, N is the total number of elements (mesh cell). In the main simulation conducted through out the paper, we used total $N = 49,152$ mesh-elements, and thus $h_{\text{est}} = 0.0045$. At a piecewise polynomial of order $d = 2$ for a approximation function it was confirmed that errors decrease with the order of $d + 1 = 3$ as theory of finite-element method suggests [82, 83]. So, we conclude that our numerical scheme is verified.

References

- [1] J. Mewis and N. J. Wagner. *Colloidal Suspension Rheology*, chapter Thixotropy, pages 228–251. Cambridge Series in Chemical Engineering. Cambridge University Press, 2011.
- [2] R. G. Larson and Y. Wei. A review of thixotropy and its rheological modeling. *Journal of Rheology*, 63:477–501, 2019.
- [3] K. Dullaert and J. Mewis. A structural kinetics model for thixotropy. *Journal of Non-Newtonian Fluid Mechanics*, 139:21–30, 2006.
- [4] J. Engmann and A. S. Burbidge. Fluid mechanics of eating, swallowing and digestion - overview and perspectives. *Food & Function*, 4:443–447, 2013.
- [5] D. Quemada and R. Droz. Blood viscoelasticity and thixotropy from stress formation and relaxation measurements: a unified model. *Biorheology*, 20:635–651, 1983.
- [6] R. G. de Krester and D. V. Boger. A structural model for the time-dependent recovery of mineral suspensions. *Rheologica Acta*, 40:582–590, 2001.
- [7] Peptide-Based Physical Gels Endowed with Thixotropic Behaviour. N. zanna and c. tomasini. *Gels*, 3:39, 2017.
- [8] S. Mortazavi-Manesh and J. M. Shaw. Thixotropic rheological behavior of maya crude oil. *Energy & Fuels*, 28:972–979, 2014.
- [9] E. Armelin, M. Martí, E. Rudé, J. Labanda, J. Llorens, and C. Alemán. A simple model to describe the thixotropic behavior of paints. *Progress in Organic Coatings*, 57(3):229–235, 2006.
- [10] H. A. Barnes. Thixotropy—a review. *Journal of Non-Newtonian Fluid Mechanics*, 70(1–2):1–33, 1997.
- [11] J. Mewis and N. J. Wagner. Thixotropy. *Advances in Colloid and Interface Science*, 147–148:214–227, 2009.
- [12] C. F. Goodeve. A general theory of thixotropy and viscosity. *Transactions of Faraday Society*, 35:342–358, 1939.
- [13] F. Moore. The rheology of ceramic slips and bodies. *Transactions and journal of British Ceramic Society*, 58:470–494, 1959.
- [14] J. Stickel, R. J. Phillips, and R. L. Powell. A constitutive model for microstructure and total stress in particulate suspensions. *Journal of Rheology*, 50:379, 2006.
- [15] J. D. Goddard. Dissipative materials as models of thixotropy and plasticity. *Journal of Non-Newtonian Fluid Mechanics*, 14:141–160, 1984.
- [16] P. D. Patel and W. B. Russel. A mean field theory for the rheology of phase separated or flocculated dispersions. *Colloids and Surfaces*, 31:355–383, 1988.
- [17] A. A. Potanin. On the mechanism of aggregation in the shear flow of suspensions. *Journal of Colloid and Interface Science*, 145:140–157, 1991.

- [18] D. S. Dickey and J. B. Fasano. How geometry and viscosity influence mixing. *Chemical Engineering*, 111:42–46, 2004.
- [19] A. B. Metzner and R. E. Otto. Agitation of nonNewtonian fluids. *AIChE Journal*, 3:3–10, 1957.
- [20] J. E. López-Aguilar, M. F. Webster, H. R. Tamaddon-Jahromi, and O. Manero. A comparative numerical study of time-dependent structured fluids in complex flows. *Rheologica Acta*, 55:197–214, 2016.
- [21] J. E. López-Aguilar, M. F. Webster, H. R. Tamaddon-Jahromi, and O. Manero. Numerical modelling of thixotropic and viscoelastoplastic materials in complex flows. *Rheologica Acta*, 54:307–325, 2014.
- [22] J. E. López-Aguilar, M. F. Webster, H. R. Tamaddon-Jahromi, and O. Manero. High-weissenberg predictions for micellar fluids in contraction–expansion flows. *Journal of Non-Newtonian Fluid Mechanics*, 222:190–208, 2015.
- [23] J. E. López-Aguilar, M. F. Webster, H. R. Tamaddon-Jahromi, and O. Manero. A new constitutive model for worm-like micellar systems – numerical simulation of confined contraction–expansion flows. *Journal of Non-Newtonian Fluid Mechanics*, 204:7–21, 2014.
- [24] P. Coussot. Yield stress fluid flows: A review of experimental data. *Journal of Non-Newtonian Fluid Mechanics*, 211:31–49, 2014.
- [25] A. N. Beris, J. A. Tsamopoulos, R. C. Armstrong, and R.A. Brown. Creeping motion of a sphere through a Bingham plastic. *Journal of Fluid Mechanics*, 1588:219–244, 1985.
- [26] J. Blackery and E. Mitsoulis. Creeping motion of a sphere in tubes filled with a Bingham plastic material. *Journal of Non-Newtonian Fluid Mechanics*, 70:59–77, 1997.
- [27] A. Tripathi and R. P. Chhabra. Drag on spheroidal particles in dilatant fluids. *AIChE Journal*, 41:728–731, 1995.
- [28] S. Tian. Wall effect for spherical partical in confined shear-thickening fluids. *Journal of Non-Newtonian Fluid Mechanics*, 257:13–21, 2018.
- [29] B. Gervang, A. R. Davies, and T. N. Phillips. On the simulation of viscoelastic flow past a sphere using spectral methods. *Journal of Non-Newtonian Fluid Mechanics*, 44:281–306, 1992.
- [30] P. Y. Huang and J. Feng. Wall effects on the flow of viscoelastic fluids around a circular cylinder. *Journal of Non-Newtonian Fluid Mechanics*, 60:179–198, 1995.
- [31] T. Ferroir, H. Huynh, and X. Chateau P. Coussot. Motion of a solid object through a pasty (thixotropic) fluid. *Physics of Fluids*, 16(3):594–601, 2004.
- [32] N. Maleki-Jirsaraei, S. Hassani, and S. Azizi. Settling of spherical objects through thixotropic fluids: A statistical approach. *Modern Applied Science*, 12:72–76, 2018.
- [33] M. M. Gumulya, R. R. Horsley, and V. Pareek. Numerical simulations of the settling behavior of particles in thixotropic fluids. *Physics of Fluids*, 26, 2014.

- [34] M. M. M. Thant, M. T. M. Sallehud-Din, G. Hewitt, C. Hale, and J. Quarini. Mitigating flow assurance challenges in deepwater fields using active heating methods. *Society of Petroleum Engineer*, 2011.
- [35] C. R. Huang and W. Fabisiak. Thixotropic parameters of whole human blood. *Thrombosis Research*, 8:1–8, 1976.
- [36] J. J. Derksen. Simulations of thixotropic liquids. *Applied Mathematical Modeling*, 35(4):1656–1665, 2011.
- [37] J. B. Freund, J. Kim, and R. H. Ewoldt. Field sensitivity of flow predictions to rheological parameters. *Journal of Non-Newtonian Fluid Mechanics*, 257, 2018.
- [38] C. M. Rodkiewicz, editor. *Arteries and Arterial Blood Flow: Biological and physiological aspects*. CISM International Centre for Mechanical Sciences. Springer-Verlag Wien, 1st edition, 1983.
- [39] A. Tehrani. Thixotropy in water-based drilling fluids. *Annual Transactions of the nordic rheology society*, 16:1–13, 2008.
- [40] J. Happel and H. Brenner. *Low Reynolds number hydrodynamics*. Prentice-Hall, London, 1965.
- [41] H. Tabuteau, P. Coussot, and J. de Bruyn. Drag force on a sphere in steady motion through a yield-stress fluid. *Journal of Rheology*, 51(1):125–137, 2007.
- [42] D. Arndt, W. Bangerth, D. Davydov, T. Heister, L. Heltai, M. Kronbichler, M. Maier, J. P. Pelteret, B. Turcksin, and D. Wells. The deal.II library, version 8.5. *Journal of Numerical Mathematics*, 2017.
- [43] W. Bangerth, R. Hartmann, and G. Kanschat. deal.II — a general purpose object oriented finite element library. *ACM Trans. Math. Softw.*, 33(4):24/1–24/7, 2007.
- [44] C. Taylor and P. Hood. A numerical solution of the navier-stokes equations using the finite element technique. *Computers & Fluids*, 1:73–100, 1973.
- [45] J. S. Hesthaven and T. Warburton. *Nodal Discontinuous Galerkin Methods: Algorithms, Analysis, and applications*. Texts in Applied Mathematics. Springer-Verlag New York, 2008.
- [46] P. Saramito. *Complex Fluids: Modeling and Algorithms*, volume 79 of *Mathématiques et Applications*. Springer, 2016.
- [47] Y. Saad and M. H. Schultz. GMRES: A generalized minimal residual algorithm for solving nonsymmetric linear systems. *SIAM Journal on Scientific Computing*, 7:856–869, 1986.
- [48] R. C. Mittal and A. H. AL-Kurdi. An efficient method for constructing an ilu preconditioner for solving large sparse nonsymmetric linear systems by the gmres method. *Computers & Mathematics with applications*, 45:1757–1772, 2003.
- [49] R. B. Bird, R. C. Armstrong, and O. Hassager. *Dynamics of Polymeric Liquids, Vol. 1: Fluid mechanics*. Wiley, 2nd edition, 1987.
- [50] D. Fraggedakis, Y. Dimakopoulos, and J. Tsamopoulos. Yielding the yield-stress analysis: a study focused on the effects of elasticity on the settling of a single spherical particle in simple yield-stress fluids. *Soft Matter*, 12(24):5378–5401, 2016.

- [51] M. M. Cross. Rheology of non-newtonian fluids: A new flow equation for pseudoplastic systems. *Journal of Colloid Science*, 20:417–437, 1965.
- [52] Howard A. Barnes. The yield stress—a review or “panta rei ”— everything flows? *Journal of Non-Newtonian Fluid Mechanics*, 81(1):133 – 178, 1999.
- [53] J. Kim, P. K. Singh, J. B. Freund, and R. H. Ewoldt. Uncertainty propagation in simulation predictions of generalized newtonian fluid flows. *Journal of Non-Newtonian Fluid Mechanics*, 271:104138, 2019.
- [54] E. Mitsoulis and J. Tsamopoulos. Numerical simulations of complex yield-stress fluid flows. *Rheologica Acta*, 56:231–258, 2017.
- [55] N. J. Balmforth, I. A. Frigaard, and G. Ovarlez. Yielding to stress: Recent developments in viscoplastic fluid mechanics. *Annual Review of Fluid Mechanics*, 46:121–146, 2014.
- [56] H. A. Ardakani, E. Mitsoulis, and S. G. Hatzikiriakos. Thixotropic flow of toothpaste through extrusion dies. *Journal of Non-Newtonian Fluid Mechanics*, 166:1262–1271, 2011.
- [57] A. N. Alexandrou, N. Constantinou, and G. Georgiou. Shear rejuvenation, aging and shear banding in yield stress fluids. *Journal of Non-Newtonian Fluid Mechanics*, 158:6–17, 2009.
- [58] R. L. Thompson, L. U. R. Sica, and P. R. S. Mendes. The yield stress tensor. *Journal of Non-Newtonian Fluid Mechanics*, 261:211–219, 2018.
- [59] M. Dinkgreve, M. M. Denn, and D. Bonn. “everything flows?”: elastic effects on startup flows of yield-stress fluids. *Rheologica Acta*, 56(3):189–194, 2017.
- [60] J. E. López-Aguilar, M. F. Webster, H. R. Tamaddon-Jahromi, and O. Manero. Predictions for circular contraction-expansion flows with viscoelastoplastic & thixotropic fluids. *Journal of Non-Newtonian Fluid Mechanics*, 261:188–210, 2018.
- [61] M. Renardy and Y. Renardy. Thixotropy in yield stress fluids as a limit of viscoelasticity. *IMA Journal of Applied Mathematics*, 3:522–537, 2016.
- [62] P. S Stephanou and G. G. Georgiou. A nonequilibrium thermodynamics perspective of thixotropy. *The Journal of Chemical Physics*, 149:244902, 2018.
- [63] S. F. Lin and R. S. Brodkey. Rheological properties of slurry fuels. *Journal of Rheology*, 29(2):147–175, 1985.
- [64] K. L. Pinder. Time dependent rheology of the tetrahydrofuran-hydrogen sulphide gas hydrate slurry. *The Canadian Journal of Chemical Engineering*, 42:132–138, 1964.
- [65] G. R. Burgos, A. N. Alexandrou, and V. Entov. Thixotropic rheology of semisolid metal suspensions. *Journal of Materials Processing Technology*, 110:164–176, 2001.
- [66] J. B. Freund and R. H. Ewoldt. Quantitative rheological model selection: Good fits versus credible models using Bayesian inference. *Journal of Rheology*, 59:667–701, 2015.
- [67] H. Jeffreys. *Theory of Probability*. Oxford University Press, 3rd edition, 1961.
- [68] X. Yang, H. Huang, and X. Lu. Sedimentation of an oblate ellipsoid in narrow tubes. *Physical Review E*, 92:063009, 2015.

- [69] I. E. Kareva and V. L. Sennitskii. Motion of a circular cylinder in a vibrating liquid. *Journal of Applied Mechanics and Technical Physics*, 42:276–278, 2001.
- [70] N. Agarwal and R. P. Chhabra. Settling velocity of cubes in newtonian and power law liquids. *Powder Technology*, 178:17–21, 2007.
- [71] T. Sarpkaya. Forces on cylinders and spheres in a sinusoidally oscillating fluid. *Journal of Applied Mechanics*, 42:32–37, 1974.
- [72] V. L. Sennitskii. Motion of a sphere in a vibrating liquid in the presence of a wall. *Journal of Applied Mechanics and Technical Physics*, 40:662–668, 1999.
- [73] L. Zhang, C. Yang, and Z-S. Mao. Numerical simulation of a bubble rising in shear-thinning fluids. *Journal of Non-Newtonian Fluid Mechanics*, 165:555–567, 2010.
- [74] W. C. Chin. *Computational Rheology for Pipeline and Annular Flow: Non-Newtonian Flow Modeling for Drilling and Production, and Flow Assurance Methods in Subsea Pipeline Design*. Elsevier Science, 2001.
- [75] Ahmed J. Ratulowski A. Hammami. *Precipitation and Deposition of Asphaltenes in Production Systems: A Flow Assurance Overview*, pages 617–660. Springer New York, New York, NY, 2007.
- [76] D. Bonn and M. M. Denn. Yield stress fluid slowly yield to analysis. *Science*, 324:1401–1402, 2009.
- [77] M. M. Denn and D. Bonn. Issues in the flow of yield-stress liquids. *Rheologica Acta*, 50(4):307–315, 2011.
- [78] P. R. S. Mendes. Thixotropic elasto-viscoplastic model for structured fluids. *Soft Matter*, 7(6):2471–2483, 2011.
- [79] C. J. Roy. Review of code and solution verification procedures for computational simulation. *Journal of Computational Physics*, 205:131–156, 2005.
- [80] S. Steinberg and P. J. Roache. Symbolic manipulation and computational fluid dynamics. *Journal of Computational Physics*, 57:251–284, 1985.
- [81] P. J. Roache. Code verification by the Method of Manufactured solutions. *Journal of Fluids Engineering*, 124:4–10, 2001.
- [82] I. Babuska and S. Szabo. On the rates of convergence of the finite element method. *International Journal for Numerical Method for Engineering*, 18:323–341, 1982.
- [83] S. Brenner and L. R. Scott. *The mathematical theory of finite element method*, volume 15 of *Texts in Applied Mathematics*. Springer-Verlag New York, 2002.